AIP | Journal of Applied Physics

# Intra- and inter-atomic optical transitions of Fe, Co, and Ni ferrocyanides studied using first-principles many-electron calculations

Shinta Watanabe, Yuki Sawada, Masato Nakaya, Masahito Yoshino, Takanori Nagasaki, Tatsuya Kameyama, Tsukasa Torimoto, Yusuke Inaba, Hideharu Takahashi, Kenji Takeshita, and Jun Onoe

Citation: Journal of Applied Physics **119**, 235102 (2016); doi: 10.1063/1.4954070
View online: http://dx.doi.org/10.1063/1.4954070
View Table of Contents: http://scitation.aip.org/content/aip/journal/jap/119/23?ver=pdfcov
Published by the AIP Publishing



# Intra- and inter-atomic optical transitions of Fe, Co, and Ni ferrocyanides studied using first-principles many-electron calculations

Shinta Watanabe,[1,a)] Yuki Sawada,[1] Masato Nakaya,[1] Masahito Yoshino,[1] Takanori Nagasaki,[1] Tatsuya Kameyama,[2] Tsukasa Torimoto,[2] Yusuke Inaba,[3] Hideharu Takahashi,[3] Kenji Takeshita,[3] and Jun Onoe[1,a)]

[1]*Department of Materials, Physics and Energy Engineering, Graduated School of Engineering, Nagoya University, Furo-cho, Chikusa-ku, Nagoya, Aichi 464-8603, Japan*

[2]*Department of Crystalline Materials Science, Graduated School of Engineering, Nagoya University, Furo-cho, Chikusa-ku, Nagoya, Aichi 464-8603, Japan*

[3]*Research Laboratory for Nuclear Reactors, Tokyo Institute of Technology, 2-12-1-N1-16 O-okayama, Meguro-ku, Tokyo 152-8550, Japan*

(Received 9 April 2016; accepted 4 June 2016; published online 17 June 2016)

We have investigated the electronic structures and optical properties of Fe, Co, and Ni ferrocyanide nanoparticles using first-principles relativistic many-electron calculations. The overall features of the theoretical absorption spectra for Fe, Ni, and Co ferrocyanides calculated using a first-principles many-electron method well reproduced the experimental one. The origins of the experimental absorption spectra were clarified by performing a configuration analysis based on the many-electron wave functions. For Fe ferrocyanide, the experimental absorption peaks originated from not only the charge-transfer transitions from $Fe^{2+}$ to $Fe^{3+}$ but also the 3*d*-3*d* intra-transitions of $Fe^{3+}$ ions. In addition, the spin crossover transition of $Fe^{3+}$ predicted by the many-electron calculations was about 0.24 eV. For Co ferrocyanide, the experimental absorption peaks were mainly attributed to the 3*d*-3*d* intra-transitions of $Fe^{2+}$ ions. In contrast to the Fe and Co ferrocyanides, Ni ferrocyanide showed that the absorption peaks originated from the 3*d*-3*d* intra-transitions of $Ni^{3+}$ ions in a low-energy region, while from both the 3*d*-3*d* intra-transitions of $Fe^{2+}$ ions and the charge-transfer transitions from $Fe^{2+}$ to $Ni^{3+}$ in a high-energy region. These results were quite different from those of density-functional theory (DFT) calculations. The discrepancy between the results of DFT calculations and those of many-electron calculations suggested that the intra- and inter-atomic transitions of transition metal ions are significantly affected by the many-body effects of strongly correlated 3*d* electrons. *Published by AIP Publishing.*
[http://dx.doi.org/10.1063/1.4954070]

## I. INTRODUCTION

Metal ferrocyanides (MFCs) have been extensively studied from both fundamental and industrial perspectives. MFCs are one of the metal-organic framework materials with many fascinating features.[1] Because MFCs can be easily synthesized by mixing metal complexes, such as nitrate, with $[Fe(II)(CN)_6]^{4-}$ aqueous solution and have a variety of electronic and spin states, these materials have been applied to functional materials such as color inks,[2] Cesium (Cs) adsorbents,[3,4] and optical recording devices.[5]

Among these functional materials, we have focused on the MFCs as an adsorbent for Platinum-group metals (PGMs), especially Ruthenium (Ru), Rhodium (Rh) and Palladium (Pd), and Molybdenum (Mo). These elements in high level radioactive liquid waste (HLLW) have a significantly negative effect on a glass melter in the vitrification process. PGMs tend to be deposited on the side and bottom walls of the glass melter, and Mo forms the compound so-called "yellow phase" in the vitrified wastes. One way to solve these issues is to remove PGMs and Mo from HLLW prior to putting them into the glass melter. MFCs are one of the most promising materials as the adsorbent for PGMs and Mo, since FeFC have been reported to be a good adsorbent for Cs. The adsorption mechanisms of PGMs and Mo to MFCs, however, remain unclear.

To clarify the adsorption mechanisms of PGMs and Mo to MFCs, it is important to understand the electronic properties of MFCs prior to their adsorptions. However, the accurate expression of the electronic structures for MFCs is quite difficult, since these properties for MFCs are significantly influenced both by the strong correlations among localized 3*d* electrons and by correlations between the electrons for adjacent metals via a cyano-group. To solve the issues, first-principles method based on the many-electron calculation is absolutely imperative.

The first-principles analysis of the electronic structure of the strongly correlated systems based on density-functional theory (DFT)[6,7] has been improved considerably. This method is quite useful for the estimation of structural,[8] electronic,[9] and magnetic[10] properties of iron compounds. MFCs, which are strongly correlated systems, have been also studied by DFT calculations using the generalized gradient approximation (GGA) + $U$ correction method or the hybrid functional method.[11–14] However, these methods are hard to

[a)]Authors to whom correspondence should be addressed. Electronic addresses: s-watanabe@nucl.nagoya-u.ac.jp and j-onoe@nucl.nagoya-u.ac.jp

discuss the multiplet structures and optical transitions between multiplets. On the other hand, first-principles analysis of these properties using the explicit many electron wave functions remains limited. One of the authors has investigated the optical properties of the strongly correlated systems, such as lanthanides-doped materials, using a first-principles many-electron method.[15–19] However, these analyses have been applied to only the inter-atomic transitions of transition metals and lanthanides.

In the present study, we have investigated the multiplet energy levels and absorption spectra including the charge-transfer (CT) state between metals for MFCs (M = Fe, Co, and Ni) using first-principles relativistic many-electron calculations. We focus on the MFCs containing $Fe^{3+}$, $Co^{3+}$, and $Ni^{3+}$, because the characteristic absorption bands at the ultraviolet-visible (UV-Vis) region are observed in the absorption spectra of these three materials.

## II. EXPERIMENTAL PROCEDURES

$K_4[Fe(II)(CN)_6]\cdot 3H_2O$ (2.11 g, 5 mmol, KANTO CHEMICAL) was dissolved in 20 ml water. This solution was added to an aqueous solution (15 ml) of metal nitrates (10 mmol, Wako 3N) and subsequently stirred for 2 h at room temperature. Then, M(III) ferrocyanides (M = Fe, Ni, and Co) were obtained in the solution. The colloidal solution was centrifuged and separated to the ferrocyanide compounds from the solution. Thereafter, the compounds were rinsed with water and centrifuged for five times. The MFC compounds thus obtained were dried at 75 °C for 12 h under atmospheric conditions and then dried in a low vacuum for 3 h.

The X-ray diffraction (XRD) patterns of the MFC (M = Fe, Co, and Ni) compounds were recorded using Rigaku Rint 2200 x-ray diffractometer (Cu Kα). UV-Vis diffuse reflectance spectra of the MFC nanoparticles were measured using Shimadzu UV-2600 spectrometer and thereafter converted to absorption spectra in terms of the Kubelka-Munk conversion equation.

## III. COMPUTATIONAL PROCEDURES

### A. Lattice parameters and atomic positions of M(III) ferrocyanide

Figure 1 shows the crystal structure of MFCs, in which divalent iron ($Fe^{2+}$) and trivalent metal ($M^{3+} = Fe^{3+}$, $Co^{3+}$, and $Ni^{3+}$) are bridged via the cyano anion group ($CN^-$). To estimate the model for relativistic many-electron calculations, we examined three different structural models: $M(III)[Fe(II)(CN)_6]^-$, $KM(III)[Fe(II)(CN)_6]$, and $CsM(III)[Fe(II)(CN)_6]$.

Since $M(III)[Fe(II)(CN)_6]^-$ has one negative charge per the primitive cell (per chemical formula), the charge neutrality is not preserved. On the other hand, the latter two models are both neutral in balance with $K^+$ and $Cs^+$ ions located at 4*c* site in $F4\bar{3}m$ symmetry, respectively. The lattice constants and atomic positions of each model were estimated by a first-principles DFT calculations using the CASTEP code,[20–22] which is based on the plane-wave basis

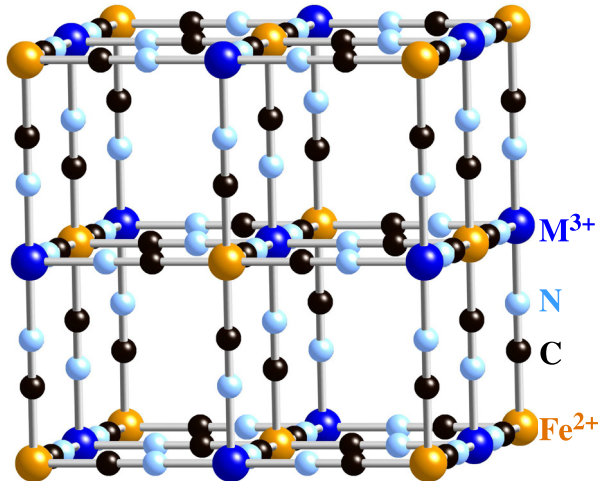


FIG. 1. Schematic illustration of the crystal structure of M(III) ferrocyanides (M = Fe, Co, Ni).

pseudopotential method. We adopted the Vanderbilt form ultrasoft pseudopotentials[23] throughout the present calculations. The exchange-correlation potential was considered within the GGA (PBE).[24] The cut-off energy for the plane wave was 550 eV, and the Brillouin zone was sampled on the $5 \times 5 \times 5$ Monkhorst–Pack grid[25] for all primitive cell calculations. All DFT calculations were performed with the GGA + *U* method based on a simplified, rotationally invariant approach.[26] We adopted different values of the *U* for the two non-equivalent 4*a* ($Fe^{2+}$) and 4*b* ($M^{3+}$) sites. These values were 3.0 eV for 4*a* ($Fe^{2+}$) site, 7.0 eV for 4*b* ($Fe^{3+}$) site, 3.0 eV for 4*b* ($Co^{3+}$) site, and 4.0 eV for 4*b* ($Ni^{3+}$) site, respectively, in reference to the previous works.[12,27] The numerical error was estimated to be less than 1 meV/atom by cut-off and *k*-point convergence tests. Geometry optimization was performed until the residual forces and stresses dropped below 0.01 eV/Å and 0.02 GPa, respectively.

### B. Multiplet energy levels and absorption spectra

The absorption spectra of MFCs were investigated using the relativistic configuration interaction (CI) method.[15,19] In this first-principles CI calculation, the multiplet energy levels and absorption spectra were calculated using $Fe^{2+}M^{3+}(CN^-)_{11}{}^{6-}$ ($M^{3+} = Fe^{3+}$, $Co^{3+}$, and $Ni^{3+}$) model cluster. The structural parameters of these model clusters were determined from the optimized structures estimated by the above method.

The details of the many-electron calculation methods were described in Refs. 15 and 19, thus we will explain the methods briefly. First, we obtained the four-component relativistic molecular orbital (MO) spinors by using relativistic DFT calculations.[28] In these relativistic DFT calculations, we adopted the relativistic formalism of the Vosko-Wilk-Nusair exchange-correlation potential $V_{xc}(\mathbf{r})$.[29,30]

After the one-electron relativistic DFT calculations, relativistic many-electron CI calculations were performed using the relativistic MO spinors. Since the CI calculations for all *N* electrons in a cluster required a prodigious quantity of computational time and resources, only MOs mainly

composed of $Fe^{2+}$–$3d$ and $M^{3+}$–$3d$ orbitals were explicitly considered in the active space. The many-electron Dirac-Coulomb-Breit Hamiltonian ($H_{DCB}$) was adopted in the present study, which can be expressed as

$$H_{DCB} = \sum_{i}^{n} h_D(\mathbf{r}_i) + \sum_{i}^{n}\sum_{j>i}^{n} \times \left[\frac{1}{r_{ij}} - \frac{1}{2r_{ij}}\left\{\boldsymbol{\alpha}_i \cdot \boldsymbol{\alpha}_j + \frac{(\boldsymbol{\alpha}_i \cdot \mathbf{r}_{ij})(\boldsymbol{\alpha}_j \cdot \mathbf{r}_{ij})}{r_{ij}^2}\right\}\right], \quad (1)$$

where $n$ is the number of electrons in the active space of the CI calculation and $\mathbf{r}_i$ is the position of the $i$th electron. The first and second terms of $H_{DCB}$ represent the one-electron and two-electron operators, respectively. The one-electron Dirac operator $h_D$ can be expressed as

$$h_D(\mathbf{r}_i) = c\tilde{\boldsymbol{\alpha}}\mathbf{p}_i + \tilde{\beta}c^2 - \sum_{\nu}\frac{Z_\nu}{|\mathbf{r}_i - \mathbf{R}_\nu|} + V_0(\mathbf{r}_i), \quad (2)$$

where $c$ is the velocity of light, $\mathbf{p}_i$ is the momentum operator, $\tilde{\boldsymbol{\alpha}}$ and $\tilde{\beta}$ are the Dirac matrices, $Z_v$ and $\mathbf{R}_v$ are the charge and position of the $v$th nucleus. $V_0(\mathbf{r}_i)$ in Eq. (2) denotes the Coulomb and exchange-correlation potential on the explicitly treated electrons from the other electrons. This potential $V_0(\mathbf{r}_i)$ was derived by our previous paper.[21] The frequency-independent Breit operator, the term following $1/r_{ij}$ in Eq. (1), represents the relativistic effects of the electron-electron repulsion.[31,32]

Many-electron wave functions are generally expressed as a linear combination of Slater determinants

$$\Psi_i = \sum_{p=1}^{M} C_{ip}\Phi_p, \quad (3)$$

where $\Psi_i$ are the $i$th many-electron wave functions, $\Phi_p$ is the $p$th Slater determinant, $C_{ip}$ is a coefficient, and $M$ is the number of Slater determinants. As the active space for the CI calculations, all the electronic configurations of the $3d$–$3d$ transitions for both $Fe^{2+}$ and $M^{3+}$ were explicitly treated. On the other hand, the electronic configurations for the CT transitions between $Fe^{2+}$ and $M^{3+}$ were considered up to two electron excitations.

The oscillator strength of the electric dipole transitions both for the $3d$–$3d$ intra-transitions of $Fe^{2+}$ and $M^{3+}$ ions and for the $Fe^{2+}$–$M^{3+}$ CT transitions averaged over all directions was obtained by using the general equation for the electric dipole transition.[33] Theoretical absorption spectra were obtained by convolution of the oscillator strength with a 0.30 eV full width at half maximum Gaussian function.

## IV. RESULTS AND DISCUSSION

### A. Crystal structure and DFT calculations for MFCs

Figure 2 shows the experimental (upperpart) and simulated (underpart) powder XRD patterns of MFCs (M = Fe, Co, and Ni): NiFC (green, top), CoFC (blue, middle), and FeFC (red, bottom). The simulated patterns were estimated by using a cubic $F4\bar{3}m$ structure. The experimental powder

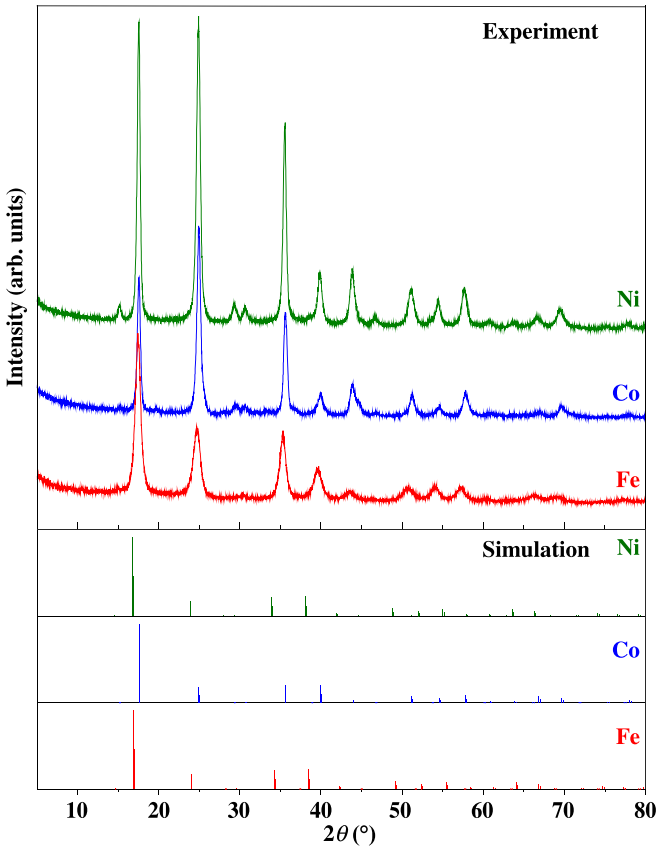


FIG. 2. Experimental (upper part) and simulated (under part) powder XRD patterns of FeFC (red line, bottom), CoFC (blue line, middle), and NiFC (green line, top) nanoparticles. The simulated Powder XRD patterns were obtained for a cubic $F4\bar{3}m$ structure.

XRD patterns indicate that the crystal structure of the synthesized MFCs is a cubic $F4\bar{3}m$ structure. The lattice constants and particle sizes of MFCs were estimated by fitting the (200) diffraction peak with the pseudo-Voigt function and by using the Scherrer equation with a constant of 0.94, respectively. We obtained the lattice constants and particle sizes to be 10.16 Å and ca. 11 nm for FeFC, 10.10 Å and ca. 19 nm for CoFC, and 10.12 Å and ca. 21 nm for NiFC, respectively. The difference of the lattice constants among three MFCs reflects the difference of the ionic radii for $Fe^{3+}$, $Co^{3+}$, and $Ni^{3+}$.

Table I summarizes the lattice constants and bond lengths for the three MFCs estimated by DFT calculations with the low spin (LS) state for $Fe^{2+}$, $Co^{3+}$, and $Ni^{3+}$, and the high spin (HS) state for $Fe^{3+}$, respectively. In addition, ferromagnetic order was considered for HS $Fe^{3+}$ and LS $Ni^{3+}$ ions. To confirm this, we examined three different types of the magnetic order proposed by Middlemiss and Wilson:[11] ferromagnetic (FM), antiferromagnetic type-I ($AF_1$), and type-II ($AF_2$). In the present DFT calculations based on the GGA + $U$ method, the difference in total energy among them was too small (less than 0.001 eV) to discuss the magnetic stability of MFCs. The magnetism of FeFC was, however, experimentally reported to exhibit ferromagnetic order at a low temperature.[34] Thus, we considered the ferromagnetic order for HS $Fe^{3+}$ to calculate the structural parameters and density of states (DOS). In addition,

TABLE I. Theoretical lattice constants and each bond lengths of the three models for MFCs. The unit of length is Å.

| FeFC | $Fe[Fe(CN)_6]^-$ | $KFe[Fe(CN)_6]$ | $CsFe[Fe(CN)_6]$ |
|---|---|---|---|
| Lattice constant | 10.470 | 10.279 | 10.306 |
| $Fe^{2+}$-C | 1.905 | 1.864 | 1.870 |
| $Fe^{3+}$-N | 2.139 | 2.086 | 2.094 |
| C-N | 1.191 | 1.189 | 1.189 |
| CoFC | $Co[Fe(CN)_6]^-$ | $KCo[Fe(CN)_6]$ | $CsCo[Fe(CN)_6]$ |
| Lattice constant | 10.114 | 9.927 | 9.962 |
| $Fe^{2+}$-C | 1.917 | 1.871 | 1.879 |
| $Co^{3+}$-N | 1.951 | 1.907 | 1.909 |
| C-N | 1.188 | 1.185 | 1.187 |
| NiFC | $Ni[Fe(CN)_6]^-$ | $KNi[Fe(CN)_6]$ | $CsNi[Fe(CN)_6]$ |
| Lattice constant | 10.552 | 10.316 | 10.352 |
| $Fe^{2+}$-C | 1.930 | 1.890 | 1.895 |
| $Ni^{3+}$-N | 2.159 | 2.083 | 2.095 |
| C-N | 1.188 | 1.185 | 1.185 |

considering the lattice constants for the three MFCs estimated by powder XRD and Shannon's ionic radii of $M^{3+}$,[35] these spin states are reasonable. The explicit spin states of MFCs can be estimated by many-electron calculations as more fully described below.

As shown in Table I, the lattice constant of $Fe[Fe(CN)_6]^-$ and $Ni[Fe(CN)_6]^-$ was overestimated by ca. 3% and 4% compared to their experimental values, respectively. This is due to the delocalization of an excess electron. On the other hand, the lattice constants for $KM[Fe(CN)_6]$ and $CsM[Fe(CN)_6]$ (M = Fe and Ni) were in reasonably agreement with the experimental one. In the case of CoFC, the lattice parameters for all the models reasonably reproduced the experimental ones. These results originate from the magnetic structure of CoFC. Compared to the spin states of FeFC and NiFC, the spin state of CoFC is quite simple. Both $Co^{3+}$ and $Fe^{2+}$ ions have $3d^6$ electric configurations with the LS state, which the $t_{2g}$ orbitals of both $Co^{3+}$ and $Fe^{2+}$ are filled. Thus, the ground state (GS) of CoFC is a nonmagnetic singlet state. Because this state can be drastically stable than other spin states, the lattice constant and localized 3*d* electrons can be correctly estimated in all three models. Since the bond length of $Fe^{2+}$-C was close to each other for all the MFCs as well as that of C-N, the difference in the lattice constant among MFCs used here is mainly caused by a change in $M^{3+}$-N bond length.

Figures 3–5 show the DOSs of FeFC, CoFC, and NiFC calculated by using the three models: (a) $M[Fe(CN)_6]^-$, (b) $KM[Fe(CN)_6]$, and (c) $CsM[Fe(CN)_6]$ (M = Fe, Co, and Ni). The Fermi level ($E_F$) is set at 0 eV along the energy axis. The occupied and unoccupied DOSs are located below and above $E_F$, respectively. The positive and negative values of DOS indicate the up and down spin states, respectively. The partial DOSs indicated by gray, blue, and red denote *s*, *p*, and *d*-orbitals, respectively.

First, as shown in parts (a)–(c) of Figs. 3–5, the insertion of $K^+$ or $Cs^+$ ion to the inner space of $M[Fe(CN)_6]^-$ (M = Fe, Co, and Ni) has no effects on their valence electronic structures for all MFCs. Especially, we focused on the energy range between the top of valence band and the lowest

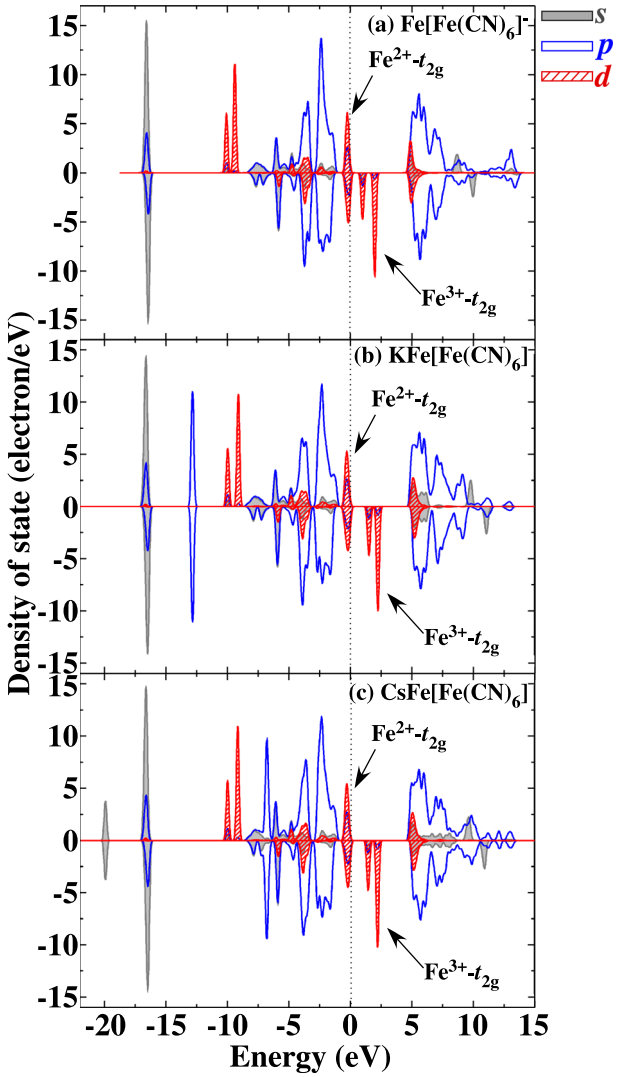


FIG. 3. The DFT-density of state (DOS) of FeFC calculated by using the three models: (a) $Fe[Fe(CN)_6]^-$, (b) $KFe[Fe(CN)_6]$, and (c) $CsFe[Fe(CN)_6]$. The Fermi level ($E_F$) is located at 0 eV along the energy axis. The occupied and unoccupied DOSs are located below and above the $E_F$, respectively. The positive and negative values of DOS indicate the up and down spin states, respectively. The partial DOSs indicated by gray, blue, and red denote *s*, *p*, and *d*-orbital, respectively.

unoccupied 3*d* orbitals of transition metals. In the case of FeFC, as shown in Fig. 3, the occupied band at near the $E_F$ consists of the $t_{2g}$ orbitals of $Fe^{2+}$, whereas the lowest unoccupied band located at ca. 1.4 eV above the $E_F$ consists of the $t_{2g}$ down spin orbitals of $Fe^{3+}$ for the three models. The electron excitations between these two occupied and unoccupied levels imply the CT transitions from the $Fe^{2+}$ occupied states to the $Fe^{3+}$ unoccupied states. Consequently, the absorption bands in the visible region of FeFC can be qualitatively attributed to the charge-transfer transitions from $Fe^{2+}$ occupied states to $Fe^{3+}$ unoccupied states. In the case of CoFC, as shown in Fig. 4, the occupied band at near the $E_F$ consists of the occupied $t_{2g}$ orbitals of $Fe^{2+}$ as is the case in FeFC, whereas the unoccupied band located at ca. 1.6–1.9 eV above the $E_F$ consists of the $e_g$ orbitals for $Co^{3+}$. This result indicates that the absorption band in the visible region of CoFC can be also attributed to the charge-transfer

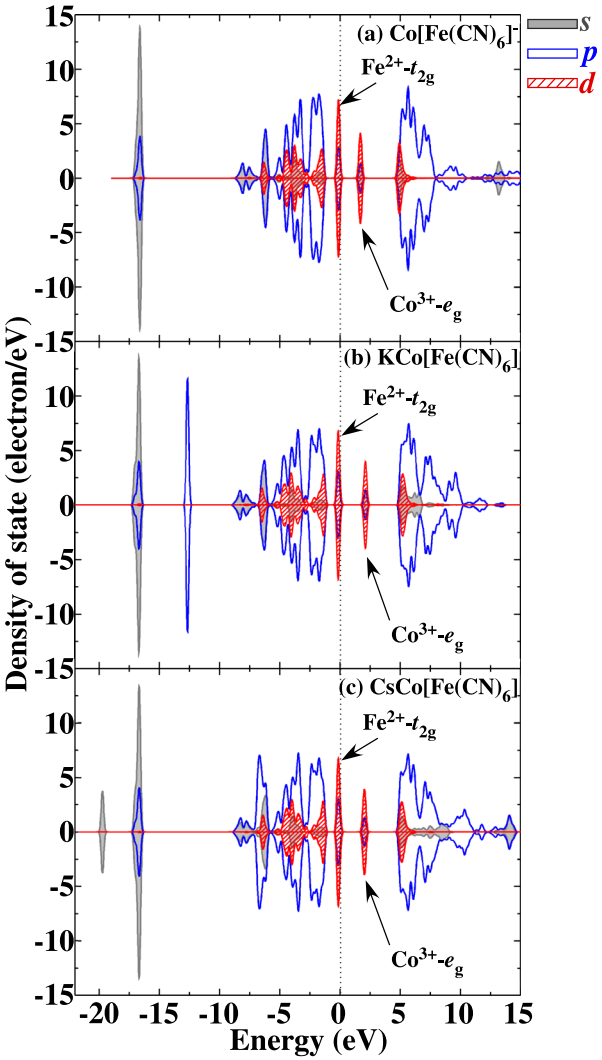


FIG. 4. The DFT-DOS of CoFC calculated by using the three models: (a) $Co[Fe(CN)_6]^-$, (b) $KCo[Fe(CN)_6]$, and (c) $CsCo[Fe(CN)_6]$, in a similar manner to Fig. 3.

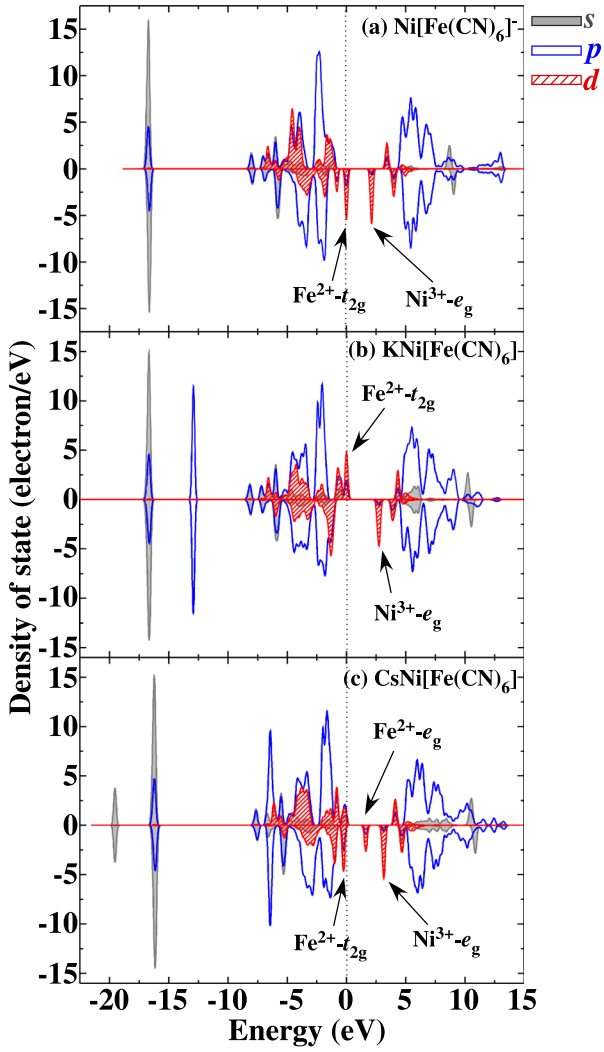


FIG. 5. The DFT-DOS of CoFC calculated by using the three models: (a) $Ni[Fe(CN)_6]^-$, (b) $KNi[Fe(CN)_6]$, and (c) $CsNi[Fe(CN)_6]$, in a similar manner to Fig. 3.

transitions from $Fe^{2+}$ occupied states to $Co^{3+}$ unoccupied states. As shown in Fig. 5, compared to the FeFC and CoFC, the electronic structures of NiFC are rather complicated. The occupied and unoccupied states at near the $E_F$ are fully miscible with the orbitals mainly composed of Fe-3*d* and Ni-3*d*. Accordingly, it is hard to assign the origins of the absorption bands appearing in the visible region clearly. This results from a difficulty to treat the strongly correlated systems in the framework of the one-electron approximation. The transitions between 3*d* orbitals basically originate in the transitions between the multiplet structures. Therefore, the analyses for the strongly correlated systems, such as MFCs, based on the explicit many electron wave functions are indispensable.

### B. Multiplet energy levels and absorption spectra: Many-electron calculations

Because the optical transitions associated with electrons in the 3*d* orbitals are strongly affected by many-body effects, the many-electron calculations using the explicit many-electron wave functions allow us to discuss the optical transitions arising from the multiplet structures. In the present work, we calculated the multiplet energy levels and absorption spectra using $Fe(II)M(III)(CN^-)_{11}^{6-}$ (M = Fe, Co, Ni) model clusters. The structural parameters of these model clusters were taken from those for the optimized bulk structures of the $CsM[Fe(CN)_6]$ (M = Fe, Ni, and Co), as shown in Table I.

Figure 6 shows the experimental (top) and theoretical (bottom) absorption spectra of FeFC. In the theoretical spectrum, the oscillator strengths of individual peaks are also shown. The overall features of the theoretical absorption spectrum well reproduced the experimental spectrum, although the absolute multiplet energy levels (transition energy) were overestimated by ca. 1.5–2.0 eV systematically. The overestimation of the multiplet energy can be corrected by performing the Slater's transition-state calculations,[36] which is shifted by the orbital energy difference between the single-electron orbitals of the Slater transition-state as a reference.[15,37] The discrepancy between the experimental and theoretical spectra may be mainly due to the electron-correlation effects of ligands. The electron-correlation effects between transition metals and ligands may be actually

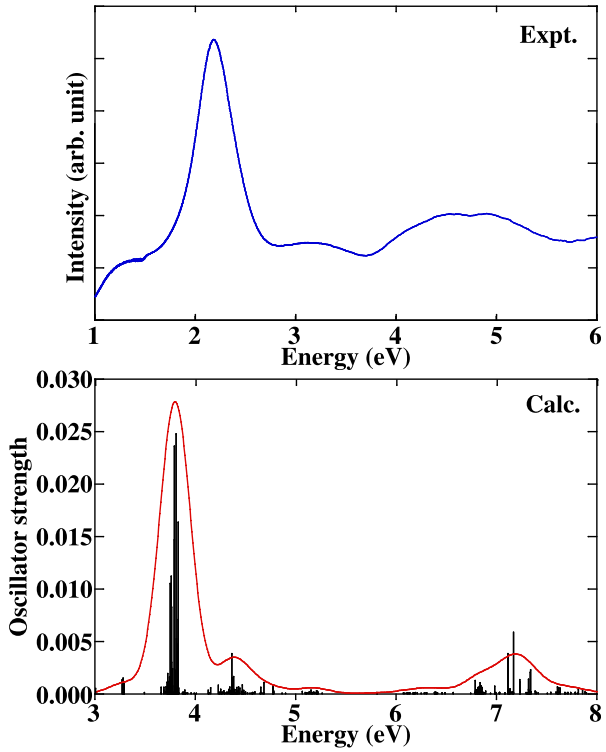


FIG. 6. Comparison between the experimental (a) and theoretical (b) absorption spectra of FeFC.

important to a rigorous estimation of the charge-transfer states between transition metals, because the transition metals in ferrocyanides are cross-linked via $CN^-$. However, since the electrons and orbitals of the ligands could not be explicitly treated as the active space because of computational costs, it is hard to consider the electron-correlation effects between transition metals and ligands at the present time. It is concern that inclusion of these effects would improve the agreement between calculated and experimental absorption spectra. These large-sized calculations are now challenging issues but may be realized in near feature.

In order to assign the individual peaks of the theoretical absorption spectrum, configuration analysis of the many-electron wave functions was performed. Fig. 7 shows both the oscillator strengths of the transitions from the lowest state and the configuration compositions for each level, together with the corresponding electronic configurations. It is noted that the electronic configurations only relevant to the absorption in the visible region are shown in Fig. 7. The Fe-3*d* levels split into the $t_{2g}$ and $e_g$ from the lower level according to the irreducible representations of $O_h$ symmetry. The main component for the GS was the $(Fe^{2+}t_{2g})^6(Fe^{2+}e_g)^0(Fe^{3+}t_{2g})^3(Fe^{3+}e_g)^2$ configuration with contribution of the $(Fe^{2+}t_{2g})^5(Fe^{2+}e_g)^0(Fe^{3+}t_{2g})^4(Fe^{3+}e_g)^2$ configuration. This result indicates that the $Fe^{2+}$ and $Fe^{3+}$ are LS and HS states for their GSs, respectively. The intense absorption band in the visible region corresponds to the transitions from the GS to the $(Fe^{2+}t_{2g})^6(Fe^{2+}e_g)^0(Fe^{3+}t_{2g})^4(Fe^{3+}e_g)^1$, $(Fe^{2+}t_{2g})^5(Fe^{2+}e_g)^0(Fe^{3+}t_{2g})^4(Fe^{3+}e_g)^2$, and $(Fe^{2+}t_{2g})^4(Fe^{2+}e_g)^0(Fe^{3+}t_{2g})^5(Fe^{3+}e_g)^2$ configurations, which correspond to the 3*d*–3*d* intra-transitions of $Fe^{3+}$ ions, the $Fe^{2+}$-$Fe^{3+}$ CT transitions, and the two-electron CT excitation states based on a shake-up process, respectively. This indicates that the intense absorption band in the visible region can be attributed not only to the CT transitions from $Fe^{2+}$ to $Fe^{3+}$ ions and but also to the 3*d*–3*d* intra-transitions of $Fe^{3+}$ ions. In addition, the energy difference of the spin-crossover for $Fe^{3+}$ ions was estimated to be ca. 0.24 eV, corresponding to the transitions from the GS $(Fe^{2+}t_{2g})^6(Fe^{2+}e_g)^0(Fe^{3+}t_{2g})^3(Fe^{3+}e_g)^2$ configuration to the $(Fe^{2+}t_{2g})^6(Fe^{2+}e_g)^0$ $(Fe^{3+}t_{2g})^5(Fe^{3+}e_g)^0$ configuration.

Figure 8 shows the comparison between the experimental (top) and theoretical (bottom) absorption spectra for CoFC. In the theoretical spectrum, the oscillator strengths of the absorption peaks are also shown in Fig. 8. The overall features of the theoretical absorption spectrum well reproduced the experimental spectrum, although the absolute multiplet energy levels were overestimated by ca. 1.5–2.0 eV, in a similar manner to the results of FeFC shown in Fig. 6. As shown in Fig. 9, the main component for the GS was the $(Fe^{2+}t_{2g})^6(Fe^{2+}e_g)^0(Co^{3+}t_{2g})^6(Co^{3+}e_g)^0$ configuration. This result indicates that $Fe^{2+}$ and $Co^{3+}$ ions have both LS states for their GSs. The intense absorption band in the visible region is due to the transitions from the GS to the $(Fe^{2+}t_{2g})^5(Fe^{2+}e_g)^1(Co^{3+}t_{2g})^6(Co^{3+}e_g)^0$ configuration, which corresponds to the 3*d*–3*d* intra-transitions of $Fe^{2+}$ ions. This result is completely different from that of FeFC. Because the components of the CT states for the GS are practically negligible, the $Fe^{2+}$-$Co^{3+}$ CT transitions cannot be observed. These results are quite different from those of DFT calculations. The results of many-electron calculations indicate that the CT transitions between $Fe^{2+}$ and $Co^{3+}$ are located at higher energy region.

Finally, we discuss the optical transitions for NiFC. Figure 10 shows the experimental (top) and theoretical (bottom) absorption spectra for NiFC. In the theoretical spectrum, the oscillator strengths of the absorption peaks are also shown in Fig. 10. The theoretical spectra reasonably reproduce the experimental one, and the energy error by ca. 1.5–2.0 eV shows the same tendency as for the other two MFCs. As shown in Fig. 11, the configuration analysis indicates that the optical transitions of NiFC are more complicated than those of FeFC and CoFC. The GS mainly consists of the $(Fe^{2+}t_{2g})^6(Fe^{2+}e_g)^0(Ni^{3+}t_{2g})^6(Ni^{3+}e_g)^1$ configuration, which corresponds to a LS state for both $Fe^{2+}$ and $Ni^{3+}$ ions. The origins of the absorption peaks are different in lower and higher energy regions. The main components of the peaks in a lower energy region less than ca. 5 eV were both the $(Fe^{2+}t_{2g})^6(Fe^{2+}e_g)^0(Ni^{3+}t_{2g})^5(Ni^{3+}e_g)^2$ and $(Fe^{2+}t_{2g})^6(Fe^{2+}e_g)^0(Ni^{3+}t_{2g})^4(Ni^{3+}e_g)^3$ configurations, which correspond to the 3*d*–3*d* intra-transitions of $Ni^{3+}$ ions. Furthermore, these transitions can be attributed to the spin crossover transitions of $Ni^{3+}$ ions. On the other hand, the main components of the absorption peaks in a higher energy region larger than ca. 5 eV were both the $(Fe^{2+}t_{2g})^5(Fe^{2+}e_g)^1(Ni^{3+}t_{2g})^6(Ni^{3+}e_g)^1$ and $(Fe^{2+}t_{2g})^5(Fe^{2+}e_g)^0(Ni^{3+}t_{2g})^6(Ni^{3+}e_g)^2$ configurations, which correspond to the $Fe^{2+}$ 3*d*–3*d* intra-transitions and the CT transitions from $Fe^{2+}$ to $Ni^{3+}$, respectively. These results are unique for NiFC. Because of these complicated origins of the optical transitions for NiFC, it is hard to assign the

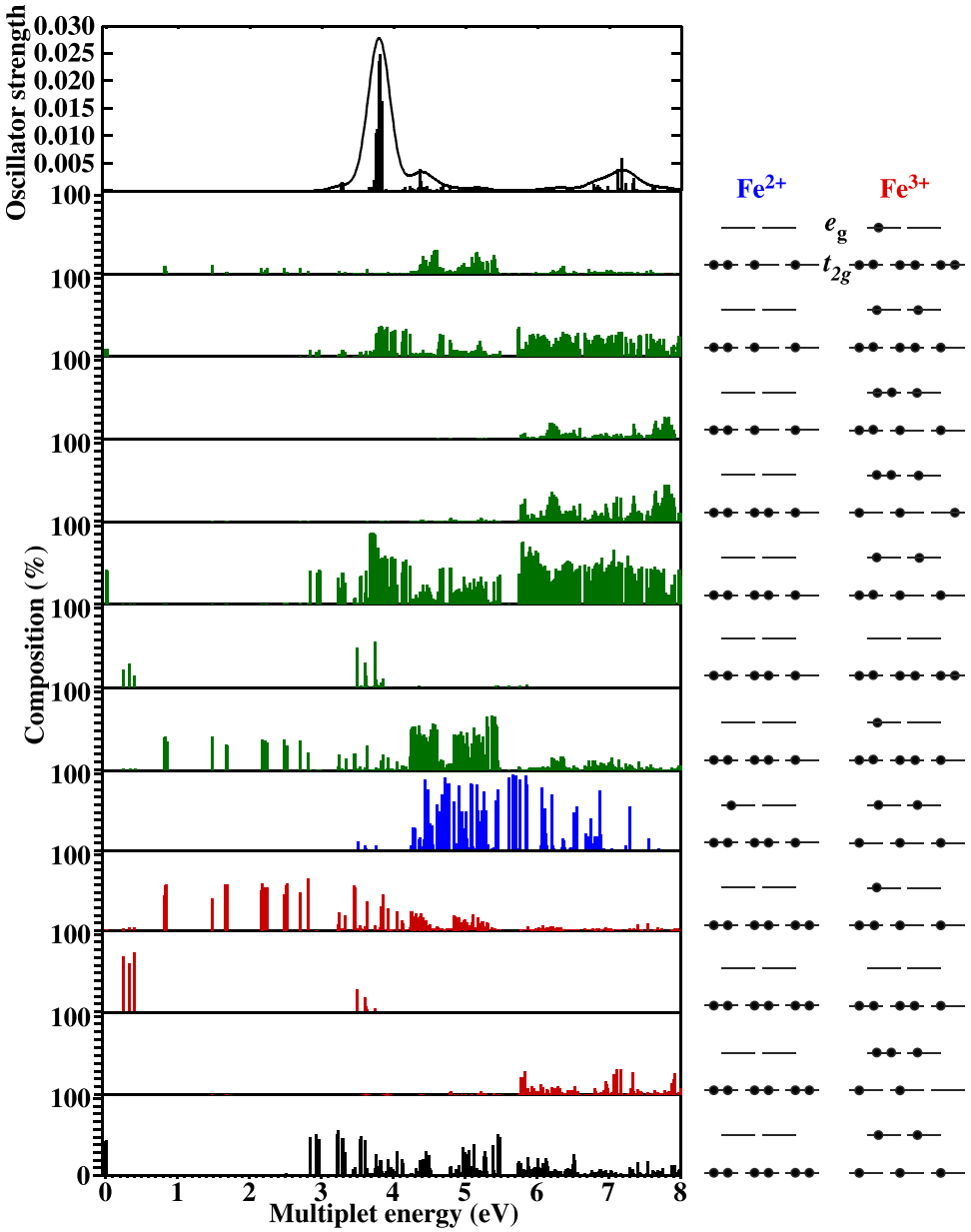


FIG. 7. Configuration analysis of the many-electron wave functions for the 3*d*-3*d* intra-transitions and $Fe^{2+}$-$Fe^{3+}$ CT transitions for FeFC. Corresponding electronic configurations are shown in the right side.

origins of the absorption bands clearly in the framework of one-electron approximations, such as DFT, as mentioned above.

For three MFCs, the results of many-electron calculations are quite different from those of DFT calculations. The discrepancy between the results of many-electron calculations and those of DFT calculations suggests that the intra- and inter-atomic transitions of transition metal ions are significantly affected by the many-body effects of strongly correlated 3*d* electrons. Consequently, the analyses based on the explicit many-electron wave functions are incredibly important to analyze the optical and electronic properties for these materials.

## V. SUMMARY

We have investigated the optical properties of M(III) ferrocyanide (M = Fe, Co, and Ni) nanoparticles, using spectroscopy and first-principles calculations. The experimental absorption spectra for the materials could be qualitatively explained using DFT calculations based on the one-electron approximation. However, more precise analyses based on the explicit many-electron wave functions are indispensable to explain the experimental spectra quantitatively.

The results of the many-electron calculations indicated that the origins of the absorption bands in the visible regions are completely different among three MFCs. In the case of FeFC, the absorption peaks in the visible region originated from not only to the CT transitions between $Fe^{2+}$ and $Fe^{3+}$ and but also to the 3*d*–3*d* intra-transitions of $Fe^{3+}$. In addition, the spin crossover transition of $Fe^{3+}$ predicted by the many-electron calculations was on the order of 0.24 eV. For the CoFC, on the other hand, the absorption peaks in visible region can be attributed to the 3*d*–3*d* intra-transitions of $Fe^{2+}$. For NiFC, in sharp contrast to the other two MFCs, the

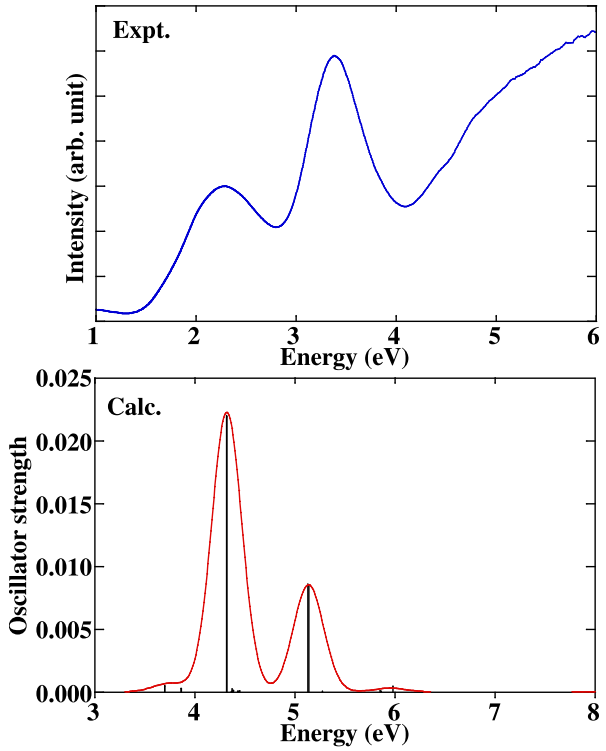


FIG. 8. Comparison between the experimental (a) and theoretical (b) absorption spectra of CoFC.

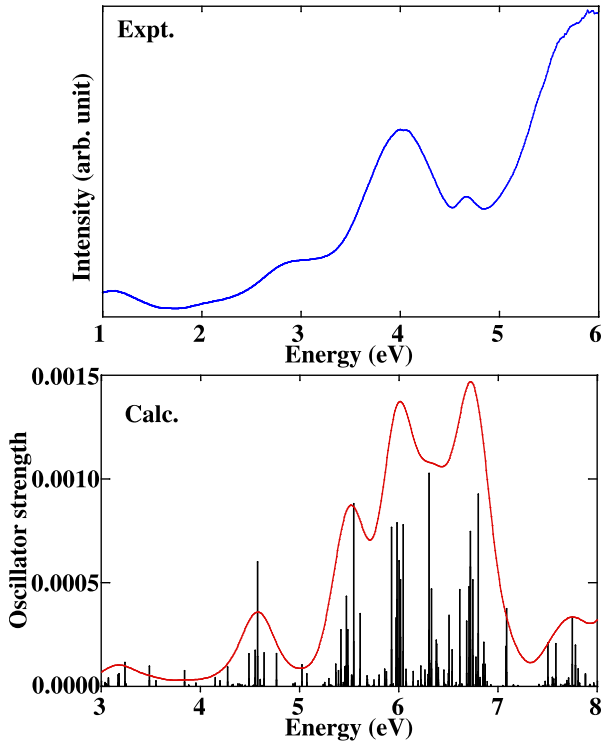


FIG. 10. Comparison between the experimental (a) and theoretical (b) absorption spectra of NiFC.

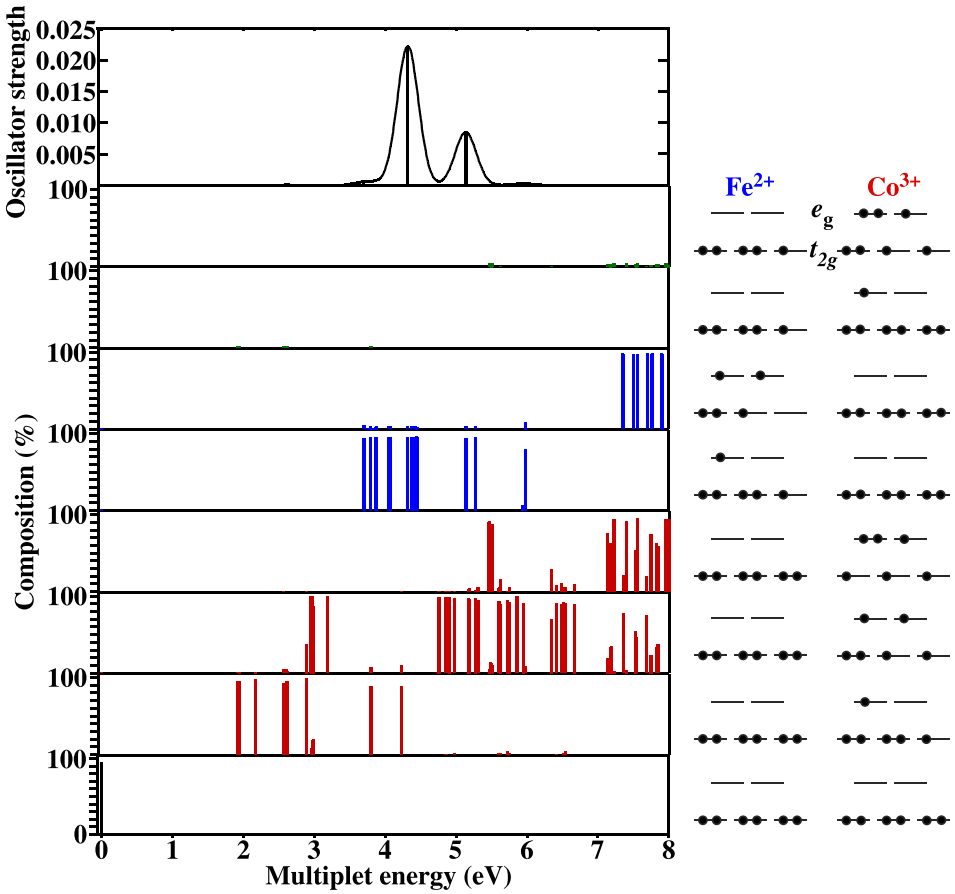


FIG. 9. Configuration analysis of the many-electron wave functions for the 3*d*-3*d* intra-transitions and $Fe^{2+}$-$Co^{3+}$ CT transitions for CoFC. Corresponding electronic configurations are shown in the right side.

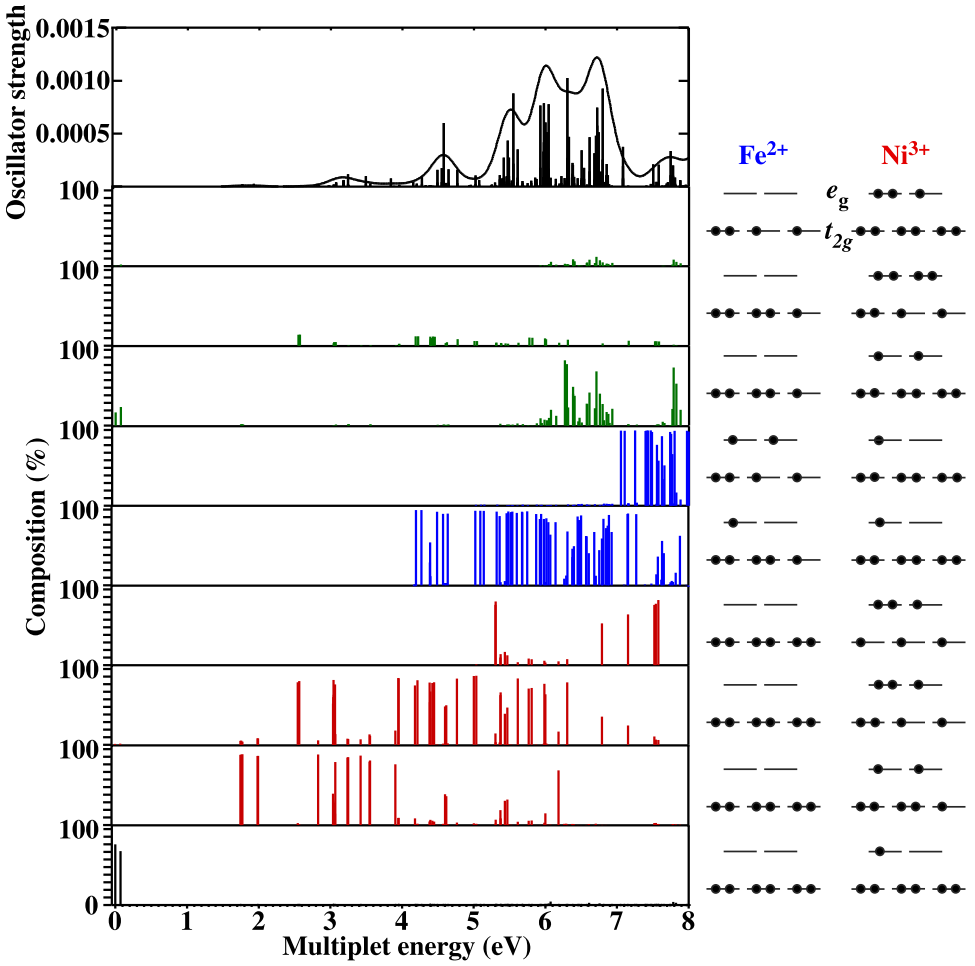


FIG. 11. Configuration analysis of the many-electron wave functions for the 3*d*-3*d* intra-transitions and $Fe^{2+}$-$Ni^{3+}$ CT transitions for NiFC. Corresponding electronic configurations are shown in the right side.

peaks at low-energy and high-energy region originated from the $Ni^{3+}$ 3*d*–3*d* intra-transitions for low-energy and the $Fe^{2+}$ 3*d*–3*d* intra-transitions and CT transitions between $Fe^{2+}$ and $Ni^{3+}$for high energy, respectively.

Finally, the present work demonstrated that first-principles many-electron calculations are a promising tool to analyze optical properties of the strongly correlated systems such as MFCs quantitatively.

## ACKNOWLEDGMENTS

The present work was financially supported by "The Initiatives for Atomic Energy Basic and Generic Strategic Research" from MEXT (Ministry of Education, Culture, Sports, Science and Technology). The DFT calculations using the CASTEP code was performed by using "Computer System for Nanostructure Design" of Nagoya University Venture Business Laboratory.

[1]S. Kitagawa, R. Kitaura, and S. Noro, Angew. Chem. Int. Ed. **43**, 2334 (2004).
[2]A. Gotoh, H. Uchida, M. Ishizaki, T. Satoh, S. Kaga, S. Okamoto, M. Ohta, M. Sakamoto, T. Kawamoto, H. Tanaka, M. Tokumoto, S. Hara, H. Shiozaki, M. Yamada, M. Miyake, and M. Kurihara, Nanotechnology **18**, 345609 (2007).
[3]J. Lehto, S. Haukka, R. Harjula, and M. Blomberg, J. Chem. Soc., Dalton Trans. **1990**, 1007.
[4]N. L. Torad, M. Hu, M. Inamura, M. Naito, and Y. Yamauchi, J. Mater. Chem. **22**, 18261 (2012).
[5]H. Tokoro and S. Ohkoshi, Bull. Chem. Soc. Jpn. **88**, 227 (2015).
[6]P. Hohenberg and W. Kohn, Phys. Rev. **136**, B864 (1964).
[7]W. Kohn and L. J. Sham, Phys. Rev. **140**, A1133 (1965).
[8]E. Gaudry, D. Gabarer, P. Sainctavit, C. Brouder, F. Mauri, J. Goulon, and A. Rogalev, J. Phys.: Condens. Matter **17**, 5467 (2005).
[9]M. Moreno, M. T. Barriuso, J. A. Aramburu, P. García-Fernández, and J. M. Garcia-Lastra, J. Phys.: Condens. Matter **18**, R315 (2006).
[10]A. N. Caruso, K. I. Pokhodnya, W. W. Shum, W. Y. Ching, B. Anderson, M. T. Bremer, E. Vescovo, P. Rulis, A. J. Epstein, and J. S. Miller, Phys. Rev. B **79**, 195202 (2009).
[11]D. S. Middlemiss and C. C. Wilson, Phys. Rev. B **77**, 155129 (2008).
[12]J. C. Wojdeł, L. de P. R. Moreira, S. T. Bromley, and F. Illas, J. Chem. Phys. **128**, 044713 (2008).
[13]J. C. Wojdeł, J. Mol. Model **15**, 567 (2009).
[14]J. J. C. Wojdeł, L. de P. R. Moreira, S. T. Bromley, and F. Illas, J. Mater. Chem. **19**, 2032 (2009).
[15]K. Ogasawara, T. Iwata, Y. Koyama, T. Ishii, I. Tanaka, and H. Adachi, Phys. Rev. B **64**, 115413 (2001).
[16]K. Ogasawara, S. Watanabe, H. Toyoshima, T. Ishii, M. G. Brik, H. Ikeno, and I. Tanaka, J. Solid State Chem. **178**, 412 (2005).
[17]K. Ogasawara, S. Watanabe, H. Toyoshima, and M. G. Brik, in *Handbook on the Physics and Chemistry of Rare Earths*, edited by K. A. Gschneidner, Jr., J. C. G. Bunzli, and V. K. Pecharsky (North-Holland, Amsterdam, 2007), Vol. 37, Chap. 231.
[18]S. Watanabe, T. Sasaki, R. Taniguchi, T. Ishii, and K. Ogasawara, Phys. Rev. B **79**, 075109 (2009).
[19]S. Watanabe, K. Ogasawara, M. Yoshino, and T. Nagasaki, Phys. Rev. B **81**, 125128 (2010).
[20]M. C. Payne, M. P. Teter, D. C. Allan, T. A. Arias, and J. D. Joannopoulos, Rev. Mod. Phys. **64**(4), 1045 (1992).
[21]M. D. Segall, P. J. D. Lindan, M. I. J. Probert, C. J. Pickard, P. J. Hasnip, S. J. Clark, and M. C. Payne, J. Phys.: Condens. Matter **14**, 2717 (2002).
[22]S. J. Clark, M. D. Segall, C. J. Pickard, P. J. Hasnip, M. I. J. Probert, K. Refson, and M. C. Payne, Z. Kristallogr. Cryst. Mater. **220**, 567 (2005).

[23]D. Vanderbilt, Phys. Rev. B **41**, 7892 (1990).
[24]J. P. Perdew, K. Burke, and M. Ernzerhof, Phys. Rev. Lett. **77**, 3865 (1996).
[25]H. Monkhorst and J. Pack, Phys. Rev. B **13**, 5188 (1976).
[26]M. Cococcioni and S. de Gironcoli, Phys. Rev. B **71**, 035105 (2005).
[27]L. Wang, T. Maxich, and G. Ceder, Phys. Rev. B **73**, 195107 (2006).
[28]A. Rosén, D. E. Ellis, H. Adachi, and F. W. Averill, J. Chem. Phys. **65**, 3629 (1976).
[29]S. H. Vosko, L. Wilk, and M. Nusair, Can. J. Phys. **58**, 1200 (1980).
[30]A. H. MacDonald and S. H. Vosko, J. Phys. C: Solid State Phys. **12**, 2977 (1979).
[31]B. G. Breit, Phys. Rev. **34**, 553 (1929).
[32]B. G. Breit, Phys. Rev. **39**, 616 (1932).
[33]S. Sugano, Y. Tanabe, and H. Kamimura, *Multiplets of Transition-Metal Ions in Crystals* (Academic, New York, 1970).
[34]A. Ito, M. Suenaga, and K. Ono, J. Chem. Phys. **48**, 3597 (1968).
[35]R. D. Shannon, Acta Crystallogr., Sect: A: Cryst. Phys., Diffr., Theor. Gen. Crystallogr. **32**, 751 (1976).
[36]J. C. Slater, *Quantum Theory of Molecules and Solids* (McGraw-Hill, New York, 1974), Vol. 4.
[37]H. Ikeno, I. Tanaka, Y. Koyama, T. Mizoguchi, and K. Ogasawara, Phys. Rev. B **72**, 075123 (2005).